Satellite drag coefficient modeling for thermosphere science and mission operations

Mehta, Piyush M.; Paul, Smriti N.; Crisp, Nicholas H.; Sheridan, Philip L.; Siemes, Christian; March, Günther; Bruinsma, Sean

DOI
10.1016/j.asr.2022.05.064

Publication date
2022

Document Version
Final published version

Published in
Advances in Space Research

Citation (APA)
Mehta, P. M., Paul, S. N., Crisp, N. H., Sheridan, P. L., Siemes, C., March, G., & Bruinsma, S. (2022). Satellite drag coefficient modeling for thermosphere science and mission operations. *Advances in Space Research*, *72*(12), 5443-5459. https://doi.org/10.1016/j.asr.2022.05.064

Available online at www.sciencedirect.com

ScienceDirect

Advances in Space Research 72 (2023) 5443–5459

ADVANCES IN SPACE RESEARCH (a COSPAR publication)

www.elsevier.com/locate/asr

Satellite drag coefficient modeling for thermosphere science and mission operations

Piyush M. Mehta [a,*], Smriti N. Paul [a], Nicholas H. Crisp [b], Philip L. Sheridan [a], Christian Siemes [c], Günther March [d], Sean Bruinsma [e]

[a] Department of Mechanical and Aerospace Engineering, West Virginia University, Morgantown, WV 26506, USA
[b] Department of Mechanical, Aerospace and Civil Engineering, The University of Manchester, Oxford Road, Manchester M13 9PL, United Kingdom
[c] Faculty of Aerospace Engineering, Delft University of Technology, Delft 2629 HS, the Netherlands
[d] RHEA for ESA – European Space Agency, Noordwijk 2201 AZ, the Netherlands
[e] CNES - Space Geodesy Office, 18 Avenue E. Belin, 31401 Toulouse, France

Received 26 January 2022; received in revised form 26 May 2022; accepted 29 May 2022
Available online 6 June 2022

Abstract

Satellite drag modeling remains the largest source of uncertainty affecting space operations in low Earth orbit. The uncertainty stems from inaccurate models for mass density and drag coefficient. Drag coefficient modeling also impacts scientific knowledge on the physics and dynamics of the upper atmosphere through the estimation of high-fidelity mass density from measurements of acceleration on-board satellites. Efforts over the last decade have pushed drag coefficient modeling in the right direction, however, have resulted in multiple methods and tools. We provide a comprehensive review of the drag coefficient modeling methods and tools. Current scale differences between thermospheric data sets mostly originate from errors in the aerodynamic modeling, specifically in the modeling of the satellite outer surface geometry and the gas-surface interactions. Enhancing these models' accuracy is intrinsically connected to the satellite drag fidelity for science and operations. A team of invested scientists recently met under the community-driven International Space Weather Action Teams (ISWAT) initiative to discuss and consolidate the efforts towards a drag coefficient modeling baseline for consistency in science and operations. In this paper, we compare the available methods for drag coefficient modeling, their impact on the derived density estimates, and make recommendations for adoption of baseline methods for science and operations. Results show that the differences in derived densities estimates can reach tens of percent at altitudes above 450 km during solar minimum conditions resulting mainly from differences in the modeling of gas-surface interactions. As a result, we conclude and recommend that robust uncertainty quantification be an integral part of any modeling efforts that employ the high-fidelity accelerometer derived density estimates. We also conclude and recommend that gas-surface interaction models that account for impact of altitude and solar variations be employed moving forward. Finally, we recommend future science missions to improve our understanding of gas-surface interactions and eventually the upper thermosphere variability.

Keywords: Atmospheric drag; Gas-surface interactions; Thermosphere; Neutral density; Satellite aerodynamics; Aerodynamic modeling

1. Introduction

Satellite drag impacts several aspects of a mission to low Earth orbit (LEO): mission design and planning, mission lifetime, orbit determination and prediction, collision risk assessment and avoidance, and satellite guidance, naviga-

* Corresponding author.
E-mail addresses: piyushmukeshmehta@gmail.com (P.M. Mehta), smritinandan.paul@mail.wvu.edu (S.N. Paul), nicholas.crisp@manchester.ac.uk (N.H. Crisp), pls0013@mix.wvu.edu (P.L. Sheridan), c.siemes@tudelft.nl (C. Siemes), gunther.march@esa.int (G. March), Sean.Bruinsma@cnes.fr (S. Bruinsma).

https://doi.org/10.1016/j.asr.2022.05.064
0273-1177/

tion, and control. Despite this clear importance, it remains the largest source of uncertainty in satellite operations. This uncertainty stems from inaccurate understanding and modeling of the satellite drag coefficient (C_D) and the variability of the thermosphere state parameters such as mass density (ρ), winds, composition and temperature. The theoretical drag model for spacecraft dynamics is given as:

$$\boldsymbol{a}_D = -\frac{1}{2}\rho\frac{C_D A}{m}V_{rel}\boldsymbol{V}_{rel} \tag{1}$$

where a_D is the drag acceleration acting on the satellite, A is the projected area perpendicular to the flow direction, m is the mass of the satellite, and V_{rel} is the velocity of the satellite relative to the co-rotating atmosphere. The largest source of error or uncertainty is ρ. For a spacecraft with a complex shape, the parameters C_D and A also can be highly uncertain. To reduce the number of uncertain parameters, some satellite properties are typically lumped into a single parameter called the ballistic coefficient ($BC = \frac{C_D A}{m}$; inverse of the standard definition in the ballistic community, $C_B = \frac{m}{C_D A}$). The velocity is generally well known from the orbit parameters and atmospheric co-rotation, however, thermospheric winds can introduce a layer of uncertainty. To make the issue more complex, the C_D is influenced by the thermosphere composition, temperature and winds. This interconnectedness of the uncertain parameters makes this an extremely challenging problem to solve.

While different approaches and strategies have been proposed to circumvent the challenge of satellite drag modeling for operations, e.g. dynamic calibration of atmosphere models (Storz et al., 2005), and simultaneous estimation of ballistic coefficient and mass density (Doornbos et al., 2008; Emmert, 2009; Mehta and Linares, 2020), they are not without limitations on their applications, nor universal. The importance of developing an accurate understanding of the physical and dynamical processes driving the uncertainty in C_D and thermosphere modeling cannot be overstated. Improved understanding of these processes will ultimately help to develop modeling resources that can be applied to all aspects of a LEO mission without limitations.

Targeted investigations over the years have revealed several important aspects about aerodynamic modeling for satellites in orbit (Moe et al., 1998; Moe and Moe, 2005; Pilinski et al., 2013; Walker et al., 2014). The aerodynamic coefficients, specifically the C_D, are influenced by several parameters that include: the free-stream temperature, molecular composition, and velocity, the surface temperature, spacecraft geometry and gas-surface interactions (GSIs). GSI is defined as the manner in which the free-stream molecules interact with the satellite surface and exchange energy and momentum. It has been shown that C_D is most sensitive to GSI (Mehta et al., 2014b; March et al., 2021) and while significant progress has been made to ascertain the true nature of GSI physics (e.g. (Walker et al., 2013; Bernstein et al., 2021)), it remains today an open question. This uncertainty is typically avoided in space operations through statistical estimation techniques.

Accelerometer derived densities estimates have been an invaluable resource for investigating the processes driving thermospheric variations (Thayer et al., 2012; Mehta et al., 2019; Xu et al., 2011; Yamazaki et al., 2015; Yang et al., 2014). They are derived through a complex process that involves isolation of the acceleration caused by drag and modeling of C_D and other parameters to back out density using. efe:drag. As a result, the uncertainty in GSI and C_D modeling is inherited by the density estimates. Multiple satellites spanning altitudes from 220 km to 500 km have carried accelerometers in the past two decades. However, because of the uncertainty in GSI and C_D modeling, several versions of the density datasets derived by different research groups across the community exist (Sutton, 2008; Doornbos, 2012; Mehta et al., 2017; March et al., 2019a). Unless relative variations were studied, this may have impacted the validity of scientific conclusions, especially when combining the datasets from different satellites. The problem becomes particularly important when modeling the thermosphere. Many different datasets, which provide the necessary spatial and temporal coverage when combined, are used in the model fit. When the datasets are not compatible, e.g. because of different GSI models used in their derivation or satellite geometry errors, modelers have to make them consistent (as accurately as possible) before adjusting the model. This is usually done by scaling the datasets, through the thermosphere model, to an accurate reference dataset. However, this is not always possible, or is associated with low accuracy, due to the absence of overlapping observations in space and time, leading to biases and errors in the thermosphere models.

To tackle these challenges, the community driven C_D modeling group was established under the International Space Weather Action Teams (ISWAT) initiative in 2019. The group has established a road map for a unified effort to address the scientific challenges and make recommendations for a baseline in C_D modeling for community adoption. This paper presents scientific results from the first comprehensive investigation into the impact of the different methods for C_D modeling on derived density estimates and makes recommendations for baseline C_D models. Specifically, we show comparisons of the different modelled C_D coefficients and the resulting density sets for the CHAMP, GRACE, and GOCE satellites. Finally, we also compare the derived density data sets with the NRLMSISE-00 (Picone et al., 2002) and DTM2020 models (Bruinsma and Boniface, 2021; Boniface and Bruinsma, 2021).

The paper is structured as follows: the next section provides a detailed description of satellite C_D including GSI models and a comprehensive review of the computational methods for estimating C_D. The next section details the process of deriving density estimates from accelerometer measurements and summarizes the various existing data-

sets. This is followed by the results and discussion section and finally the conclusions and recommendations are provided.

2. Physical drag coefficient

The C_D is a component of a more general aerodynamic coefficient, and characterizes the scaled drag force in the direction of satellite motion. In the context of spacecraft dynamics, the C_D is generally characterized as either fixed, fitted, or physical. Fixed C_D uses a predetermined value that does not change. Fitted C_D is derived using some form of a fitting or filtering process and is typically updated over time (every few hours or orbits). Physical C_D is computed by modeling the momentum and energy exchange between the flow-field particles and the satellite. It is a function of various parameters as described in the introduction. In this work, we limit our discussion to physical C_D unless otherwise stated.

2.1. Gas-surface interaction

Most satellites in low Earth orbit (LEO) encounter free molecular flow (FMF), where inter-molecular collisions are so infrequent that they can be safely neglected for the purposed of C_D modeling. The exchange between the flow-field and the satellite is then dominated by the interactions at the surface of the satellite, otherwise known as GSI. Under FMF conditions, the incoming velocity distribution is well-known. As a result, the primary unknown is the outgoing velocity distribution which is determined by i) the level of energy and momentum accommodation, and ii) the angular scattering distribution of the molecules from the surface. The basics of computing free-molecular aerodynamics based on the outgoing velocity distribution are covered in the literature (Sentman, 1961; Bird, 1994; Pilinski et al., 2010; Walker et al., 2014).

The energy and momentum exchange are modeled using the phenomenological energy and momentum accommodation coefficients, respectively. Traditionally there are three accommodation coefficients that control a GSI model: energy accommodation coefficient (α), and the normal (σ_n) and tangential (σ_t) momentum accommodation coefficient. The thermal or energy accommodation coefficient is given as

$$\alpha = \frac{E_i - E_r}{E_i - E_s} = \frac{T_{k,i} - T_{k,r}}{T_{k,i} - T_s} \tag{2}$$

where E_i and E_r are the kinetic energies of the incoming and reflected particles, respectively, while E_s is the energy corresponding to the satellite surface that the reflected particle carries away in the case of complete thermal equilibrium or accommodation ($\alpha = 1$). Similarly, $T_{k,i}$ and $T_{k,r}$ represent the kinetic temperatures of the incident and reflected particle while T_s represents the temperature of the satellite surface. While the true nature of the physical processes driving the GSIs in FMF is an active area of research, analysis of in situ measurements has resulted in a hypothesis that the abundance of the highly reactive atomic oxygen in the vicinity of the satellite influences the energy (and momentum) exchange (Moe and Moe, 1969) making possible partial energy accommodation (values of α between 0 and 1). The momentum accommodation coefficients are given as

$$\sigma_n = \frac{p_i - p_r}{p_i - p_s} \tag{3}$$

and

$$\sigma_t = \frac{\tau_i - \tau_r}{\tau_i} \quad \text{with} \quad \tau_s = 0 \tag{4}$$

where the normal momentum exchange is analogous to the energy exchange with p being normal momentum. τ_i and τ_r are incident and reflected tangential momentum.

The two extreme cases ($\alpha = \sigma_n = \sigma_t = 0$) and ($\alpha = \sigma_n = \sigma_t = 1$) represent the two extremes in reflection scattering kernels, specular and diffuse, respectively. Several different complex scattering kernels have been studied and developed for behaviour spanning the range from specular to diffuse. The most common ones include the Maxwell, diffuse (with incomplete accommodation), and quasi-specular reflections kernels. The Maxwell kernel assumes a fraction of reflections are specular while the rest are diffuse. The quasi-specular kernel models a reflection distribution (lobal pattern) about the specular direction. Fig. 1 shows the schematic of the different reflection kernels.

2.1.1. Accommodation coefficient models

Based on the hypothesis that adsorption of atomic oxygen onto the satellite surface influences GSIs, several different models have been developed for α. All existing models are empirical in nature and use fitted C_D for satellites with compact shapes to invert or infer the value of α. In the original work by Pilinski et al. (2010), a Langmuir isotherm was fitted to the inferred α as a function of the partial pressure of atomic oxygen. The reflection kernel was assumed to be diffuse. We refer to such models as diffuse reflection with incomplete accommodation (DRIA) models. A limitation of the model was that there was no lower boundary accounting for the satellite surface properties. Specifically, the value of α was allowed to fall to zero in the absence of atomic oxygen. However, according to Goodman's model (Goodman, 1977), the value of α in the absence of atomic oxygen should be dictated by the surface properties of the satellite. Goodman's model gives α for the clean or uncovered surface as

$$\alpha_s = \frac{K_s \mu}{(1+\mu)^2} \tag{5}$$

where μ is the ratio of the mass of the free stream particle to that of the surface material, and the value of K_s can lie between 2.4 and 3.6 depending on the shape of the satellite with the choice generally left to the user. As a result, the

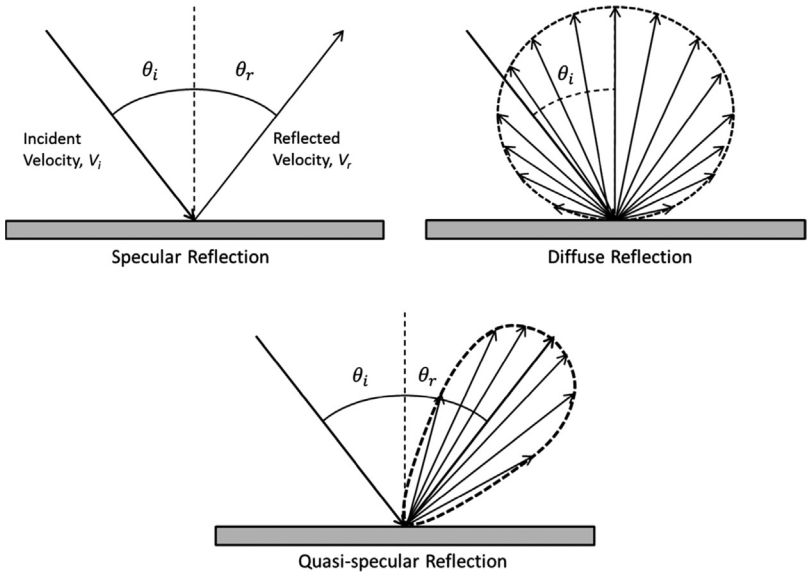

Fig. 1. Visualization of the reflections kernels.

original model was updated by Pilinski et al. (2013), who fitted a Langmuir isotherm to the fractional coverage of atomic oxygen (θ) as a function of partial pressure of atomic oxygen. This is achieved under the notion of 'effective' α such that

$$\alpha_{eff} = (1-\theta)\alpha_s + \theta\alpha_{ads} \tag{6}$$

where α_s is given by Goodman's model and α_{ads} is the accommodation coefficient for the fraction covered by the adsorbed atomic oxygen and is assumed to be unity ($\alpha_{ads} = 1$). This is one of the models we use in this work and will henceforth be referred to as the Semi-empirical Satellite Accommodation Model (SESAM).

Another approach to inverting the fractional coverage, analogous to the idea of α_{eff}, was recently developed by Walker et al. (2014)

$$C_{D,T} = (1-\theta)C_{D,s} + \theta C_{D,ads} \tag{7}$$

where $C_{D,s}$ is the drag coefficient due to the fraction that is uncovered and corresponds to the surface accommodation and $C_{D,ads}$ is the drag coefficient contribution due to the fraction that is covered by the adsorbate. Walker et al. (2014) developed two different models using this approach, one for diffuse and the other for quasi-specular reflection kernels. In this work, we use both of these models (diffuse and CLL) and will henceforth refer to them as Walker models.

The quasi-specular model is developed for use with the Cercignani-Lampis-Lord (CLL) model parameters (Lord, 1991). The CLL GSI model is controlled by two accommodation coefficients: the normal energy accommodation coefficient, α_n, and the tangential momentum accommodation coefficient, σ_t. Based on literature, previous work assumed that σ_t is unity for FMF leaving α_n as the driving parameter in the CLL model (Comsa et al., 1980; Suetin et al., 1973; Porodnov et al., 1974). Based on previous research, it is thought that α, and hence α_n, approaches unity when interacting with a surface that is covered by atomic oxygen (Moe et al., 1995). Furthermore, the total energy accommodation coefficient is the average of the normal and tangential energy accommodation coefficients

$$\alpha = \frac{\alpha_n + \alpha_t}{2} \tag{8}$$

In the CLL model, α_t is unity when σ_n is unity. Therefore, $C_{D,ads}$ is calculated by using unity for both α_n and σ_t, which yields

$$\alpha_n = 2\alpha - 1 \quad = 2\alpha_s - 1. \tag{9}$$

Combining Eqs. (5) and (9), we get

$$\alpha_n = \frac{2K_s\mu}{(1+\mu)^2} - 1. \tag{10}$$

Working with elongated shapes, we use a K_s value of 3.0 for all the satellites as in previous work (Mehta et al., 2017). Additionally, because of the approaches used in the development of all the accommodation coefficient models, a common limitation for all models is that they are only valid for use with the background thermosphere model used in the orbit fitting and model development process, specifically the NRLMSISE-00 model (Picone et al., 2002).

2.2. Computational methods

Obtaining accurate estimates of C_D for satellites with complex geometry, such as those used in this work, requires employing the correct computational method. The choice of computational method depends on the characterization of flow-field. Most of the spacecraft in LEO encounter FMF where inter-molecular collisions in the flow-field are so rare that GSIs dominate.

Most computational methods can be classified as analytical or numerical. Analytical methods include closed-form solutions for basic shapes (e.g. flat-plate, sphere, cube, etc.) (Sentman, 1961; Walker et al., 2014) and the panel method that decomposes a complex satellite geometry using flat facets where the overall C_D is assumed to be given by the sum of the contributions of the various facets. Traditionally, the major limitations of the panel method have been the inability to model flow shadowing and multiple particle reflections, however, work is currently underway to alleviate these limitations (Fredo and Kaplan, 1981; Fuller and Tolson, 2009). In this work, we use ADBSat, a tool recently developed at the University of Manchester that is described in a dedicated section below.

Numerical methods for FMF track the movement of a large number of particles, representative of the real particles in the flow-field, through their interaction with the satellite placed in the domain. These methods include the Direct Simulation Monte Carlo (DSMC) (Bird, 1994) and Test Particle Monte Carlo (TPMC) (Davis, 1960) techniques. Because numerical methods are computationally expensive, some form of mathematical/regression modeling is generally required (e.g. interpolation (March et al., 2019a) or Gaussian Process Regression (Mehta et al., 2014a)). Both techniques have been commonly employed in the community as well as in this work, and are described in detail in sections below. Because we work with complex shapes, we will limit our discussion to the panel method and numerical techniques. Fig. 2 shows the computer aided design (CAD) satellite geometry models for CHAMP, GRACE, and GOCE that have been used with the different computational methods. Detailed information about the three satellites is provided in Section 4.

2.2.1. Panel method and ADBSat

Panel methods for calculation of aerodynamic coefficients operate by reducing a geometric model of the body into a number of smaller elements (often triangular flat-plates; Fig. 3), for which the individual aerodynamic contribution can be calculated using simple analytical methods. These individual contributions can subsequently be summed together to generate the total aerodynamic coefficients for the body. Due to the use of closed-form analytical representations of the underlying GSI models applied to each element individually, panel methods are unable to account for particle–particle interactions or multiple particle reflections from surfaces (i.e. each surface is treated independently). Shadowing or shielding effects are similarly difficult to account for due to the simplicity of the method in the handling of the geometry. Panel methods, whilst computationally efficient due to their analytical basis, are therefore only suitable for the analysis of generally convex geometries with simple external features.

ADBSat (originally Aerodynamic Database for Satellites) is a panel method implementation that has been developed at The University of Manchester (Mostaza-Prieto, 2017; Sinpetru et al., 2022a; Sinpetru et al., 2022b) that enables generalised mesh import of satellite geometries and flexible application of different GSI models. A basic shadowing analysis has also been developed for ADBSat that can account for surface shielding from the flow by upstream parts of the geometry. However, this relies upon the hyperthermal flow assumption and therefore may be associated with errors at low speed ratios (i.e. higher altitudes).

ADBSat takes as input a standard geometry definition file (OBJ format) containing the vertex and face definitions of a pure triangular surface mesh describing the external geometry of the satellite. This can be developed from most suitable CAD geometries and can be simply converted from similar STL file formats. Surface texture information can also be contained in this input file, allowing for definition of multiple surface materials that can be related to different surface accommodation coefficients within ADBSat. Beyond providing an appropriate representation of the external surface geometry (see Fig. 3), the density or level of refinement of the surface mesh can be important in the application of the shadowing method (i.e. elements can either be shadowed or not-shadowed) (Sinpetru et al., 2022a; Sinpetru et al., 2022b).

Following the processing of the input mesh geometry, the aerodynamic coefficients for each triangular mesh ele-

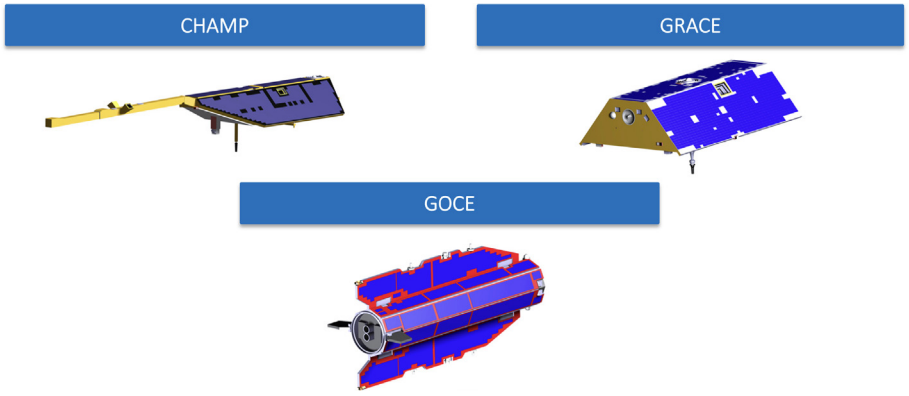

Fig. 2. Satellite Geometry Models.

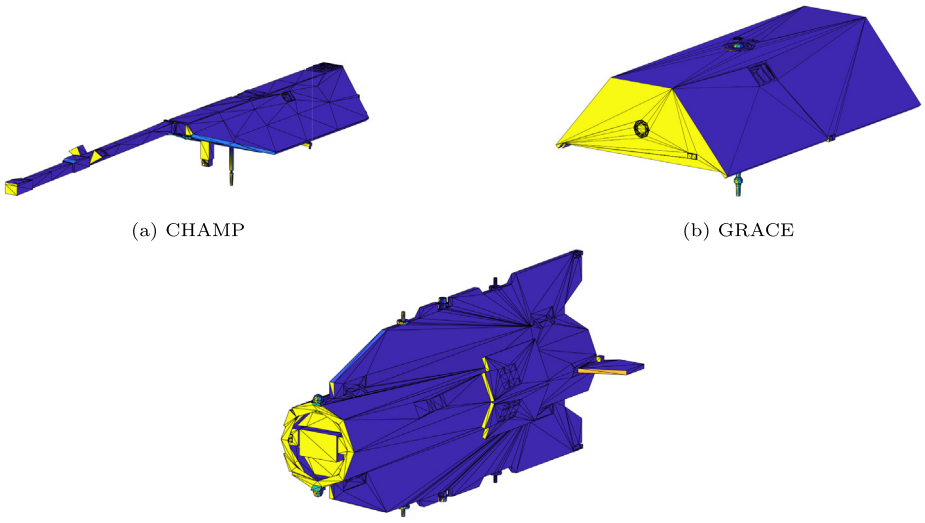

(a) CHAMP (b) GRACE

(c) GOCE

Fig. 3. Satellite geometry models as output by ADBSat. The triangular elements are coloured based on the magnitude of the surface pressure coefficient assuming a flow-aligned attitude.

ment are calculated using the chosen GSI model. A number of different GSI models have been implemented in ADBSat using available closed-form analytical solutions, including Sentman, Schaaf & Chambre, DRIA, and CLL. The modular structure of ADBSat allows the simple integration of further GSI models with closed-form solutions models in the future. At present the accommodation coefficients (associated with each material defined in the mesh) are provided as user-defined inputs to ADBSat as required by the chosen GSI model.

2.2.2. Direct simulation Monte Carlo

The Stochastic Parallel Rarefied-Gas Time-Accurate Analyzer (SPARTA) simulator from SANDIA Laboratories (Gallis et al., 2014) was used to determine the aerodynamic forces over a given satellite geometry. Among the simulation inputs, the atmosphere was 100% atomic oxygen and atmospheric and wall temperatures were 1000 K and 400 K, respectively, as described in March et al. (2019a). The chemical composition was set to 100% atomic oxygen to define the aerodynamic output associated to different speed ratios. The generated dataset for multiple speed ratios can then be used to simulate alternative and realistic mass compositions according to the chemistry inputs from atmospheric models. As the satellites of interest are at altitudes well within the FMF regime, particle–particle collisions were neglected. The GSIs were modeled as DRIA, where α was set to the carefully selected constant values of 0.85 and 0.82 for the CHAMP and GOCE satellites, respectively (March et al., 2019b). Due to a lack of a more detailed analysis, the α value for the GRACE satellites was simply selected to be the same as CHAMP. The simulations were performed for speed ratios between 0.5 and 14, which cover the entire range of speed ratios encountered along the satellite orbits in the atmosphere as specified by the NRLMSISE-00 model (Picone et al., 2002). Further, the simulations were performed for the full range of attack and sideslip angles that was encountered in orbit, where the sampling of the angles was selected to be very dense (1° steps) around the nominal attitude of 0° attack and sideslip angles, and coarser otherwise (tens of degrees steps). The resulting coefficients were then interpolated to a regular grid with 1° steps for attack and sideslip angles using a spline interpolation technique, and stored in a lookup table with three lookup columns (speed ratio, attack, and sideslip angle), which may be interpolated linearly without introducing notable interpolation errors. Such lookup tables were generated for a sequence of α values, ranging from zero to unity. When using the lookup tables to calculate density, the speed ratio is first defined for each atmospheric species. Then, the C_D is interpolated for each speed ratio, and the mass weighted average of the resulting C_D is taken.

2.2.3. Test particle Monte Carlo

The TPMC technique was developed by Klinkrad et al. (Klinkrad et al., 1990) and can model the effects of multiple reflections caused by concave geometries and flow shadowing. It is computationally less expensive for FMF than DSMC while being just as accurate. The test particles, which represent real molecules, are sequentially fired into the computational domain. Each test particle represents a large number of real molecules. The molecules are fired with velocities that are probabilistically determined. The velocity is composed of a constant free-stream bulk velocity and the probabilistically determined thermal velocity. The test particles interact with the surface but do not undergo intermolecular collisions. This work uses an in-house TPMC code developed at the Los Alamos National Laboratory (LANL) that can simulate different GSI mod-

els for energy and momentum exchange, including DRIA and CLL.

While TPMC can provide accurate estimates of C_D, like DSMC, it is also computationally too expensive for real-time application or applications that involve a substantial amount of data processing, as in the case of deriving density estimates from accelerometer drag measurements. To overcome this computational limitation, the original Response Surface Model (RSM) toolkit (Mehta et al., 2014a) was also developed at LANL and then updated/extended at West Virginia University (WVU) (Sheridan et al., 2022).

Response surface modeling, in this case Gaussian process regression (GPR), is an accurate and robust supervised machine learning technique which is ideally suited to smaller datasets. It is a nonparametric approach (i.e. does not take a functional form such as a polynomial) that calculates the probability distribution over all admissible functions that fit the data rather than calculating the probability distribution of parameters of a specific function. The output is assumed to have a multivariate Gaussian distribution, where the characteristics of the Gaussian model are dictated by the functional form of the covariance matrix or kernel. The training phase optimizes the free parameters of the covariance kernel such that the multivariate Gaussian best describes the distribution of the observed data points. GPR characterizes the response of a system or variable to changes in input conditions and can be used to predict the variable at a new set of input conditions using the posterior conditional probability. The advantage of GPR is that it inherently and accurately characterizes the uncertainty associated with predictions. Uncertainties are the smallest close to observed data points, larger when interpolating, and largest for extrapolation, which is intuitive.

The original LANL RSM toolkit used an in-house optimizer for GPR developed in MATLAB that did not have the capability to output the uncertainty associated with a prediction. One of the extensions made possible in the WVU RSM toolkit is the ability to use freely available Python libraries for GPR that also provide reliable uncertainty estimates with the prediction of C_D (Sheridan et al., 2022).

2.3. Nomenclature

Because we are working with various different models, techniques, and parameters, we develop a nomenclature scheme that we will use throughout the remainder of the paper. The acronyms for the various quantities are provided in Table 1. The nomenclature scheme is formed of the method for C_D computation, reflection model or kernel, and accommodation model/value, for example DUT-DRIA-0.85 or RSM-CLL-WLK. For clarity, DUT uses DSMC generated aerodynamic coefficient tables with interpolation and RSM uses the Gaussian process model developed from TPMC simulations. The SESAM model provides both the values of θ and α_{eff} for diffuse reflection. Walker models provide only θ for both diffuse and quasi-specular (CLL) reflection.

Table 1
Acronyms for Nomenclature.

Acronym	Description
DUT	Direct Simulation Monte Carlo + Interpolation
RSM	Test Particle Monte Carlo + Gaussian Process Regression
ADB	ADBSat Flat Panel Method
DRIA	Diffuse Reflection with Incomplete Accommodation
CLL	Cercignani Lampis Lord/ Quasi-Specular
(α =)0.85	Constant Energy Accommodation Coefficient of 0.85
SESAM	Semi-Empirical Satellite Accommodation Model
WLK	Walker Accommodation Models

2.4. Drag coefficient calculation

For RSM-DRIA-WLK and RSM-CLL-WLK, the $C_{D,T}$ is the combination of a clean surface contribution $C_{D,s}$ (i.e., a uncontaminated surface) and an adsorbate part $C_{D,ads}$ (i.e., a surface covered by atomic oxygen). The $C_{D,s}$ and $C_{D,ads}$ are obtained from the drag coefficients of atmospheric constituent species (H, He, N, N_2, O, O_2) using

$$C_{D,s} = \frac{\sum_{k=1}^{6} \chi_k m_k C_{D,s_k}}{\sum_{k=1}^{6} \chi_k m_k} \tag{11a}$$

$$C_{D,ads} = \frac{\sum_{k=1}^{6} \chi_k m_k C_{D,ads_k}}{\sum_{k=1}^{6} \chi_k m_k} \tag{11b}$$

where χ_k is the mole fraction of species k, m_k is the mass of species k, C_{D,s_k} is the surface drag coefficient corresponding to species k, and C_{D,ads_k} is the adsorbate drag coefficient corresponding to species k. The mole fraction χ_k can be computed using:

$$\chi_k = \frac{n_k}{\sum_{i=1}^{6} n_i} \tag{12}$$

where n_i is the number density of the i^{th} species. We use the NRLMSISE-00 density model for obtaining the number densities.

The inputs or independent variables for the computation of C_{D,ads_k} and C_{D,s_k} corresponding to RSM-DRIA-WLK and RSM-CLL-WLK are listed in Table 2. The parameter μ_k is the ratio of the mass of species k to the mass of the particles that compose the satellite surface. We refer to the latter quantity as surface mass, the estimation of which is discussed shortly.

For the CHAMP satellite, we assume that 50% of the surface is composed of thermal multilayer insulation

Table 2
Inputs for RSM-DRIA-WLK and RSM-CLL-WLK.

Input Description	RSM-DRIA-WLK Applicability (Yes/No); C_{D,ads_k}	RSM-CLL-WLK Applicability (Yes/No); C_{D,ads_k}	RSM-DRIA-WLK Applicability (Yes/No); C_{D,s_k}	RSM-CLL-WLK Applicability (Yes/No); C_{D,s_k}
Magnitude of relative velocity of the satellite V_{rel}	Yes	Yes	Yes	Yes
Satellite surface temperature T_w	Yes (=400 K)	Yes (=400 K)	Yes (=400 K)	Yes (=400 K)
Atmospheric temperature T_a	Yes	Yes	Yes	Yes
Energy accommodation coefficient α	Yes (=1)	No	Yes (= $3\mu_k/(1+\mu_k)^2$)	No
Normal energy accommodation coefficient α_n	No	Yes (=1)	No	Yes (larger of 0 or $2\times(3\mu_k/(1+\mu_k)^2)$-1)
Tangential momentum accommodation coefficient σ_t	No	Yes (=1)	No	Yes (=1)
Satellite yaw β and satellite pitch Φ	Yes	Yes	Yes	Yes

(MLI/Kapton), and the remaining half consists of solar panels (gallium arsenide). This assumption for the surface materials results in a surface mass of approximately 263 for CHAMP. For the GOCE satellite, we make the assumption that the entire surface consists of solar panels (gallium arsenide), which results in a surface mass of approximately 145. The publicly available "product specification document" of the GRACE satellite (Bettadpur, 2012) provides details of the areas and materials of various panels constituting the surface. Using area-based averaging, we obtain the surface mass of approximately 120 for GRACE.

For both RSM-DRIA-WLK and RSM-CLL-WLK, the parameter θ, see Eq. (7), defines the individual contributions of the adsorbate and surface drag coefficients to the total drag coefficient. The parameter θ is obtained as

$$\theta = \frac{k_L P_O}{1 + k_L P_O} \tag{13}$$

where k_L is the Langmuir adsorbate constant and P_O is the partial pressure of atomic oxygen. The value of k_L for the DRIA GSI model is 1.44×10^6, and k_L for the CLL GSI model is 2.89×10^6 (Walker et al., 2014). The partial pressure of atomic oxygen is obtained as

$$P_O = n_D \times \chi_O \times T_a \times k_B \tag{14}$$

where n_D is the total number density of the atmospheric constituents (H, He, N, N_2, O, O_2), χ_O is the mole fraction of atomic oxygen, T_a is the atmospheric temperature at the satellite position, and k_B is the Boltzmann constant.

For RSM-DRIA-SESAM, the total drag coefficient is computed as

$$C_{D,SESAM} = \left(\frac{1}{\sum_{k=1}^{6} (\chi_k m_k)} \right) \sum_{k=1}^{6} (\chi_k m_k C_{D,SESAM_k}) \tag{15}$$

where χ_k is the mole fraction of species k (obtained from the NRLMSISE-00 density model), m_k is the mass of species k, and $C_{D,SESAM_k}$ is the drag coefficient corresponding to species k.

The independent variables required as inputs for the computation of $C_{D,SESAM_k}$ are given in Table 3.

The method for computing α_{eff_k} is given as

$$\alpha_{eff_k} = (1 - \theta_{SESAM})\alpha_{s_k} + \theta_{SESAM} \tag{16}$$

where θ_{SESAM} is the fraction of satellite covered by the adsorbate, and it is given as

$$\theta_{SESAM} = \frac{k_{L_{SESAM}} P_{O_{SESAM}}}{1 + k_{L_{SESAM}} P_{O_{SESAM}}} \tag{17}$$

where $k_{L_{SESAM}}$ is the Langmuir parameter for SESAM and $P_{O_{SESAM}}$ is the partial pressure of atomic oxygen. The partial pressure, $P_{O_{SESAM}}$, is obtained as

Table 3
Inputs for $C_{D,SESAM_k}$ Corresponding to RSM-DRIA-SESAM.

Input Description	Symbol
Magnitude of relative velocity of the satellite	V_{rel}
Satellite surface temperature	T_w (=400 K)
Atmospheric temperature	T_a
(Effective) energy accommodation coefficient for species k	α_{eff_k}
Satellite yaw and satellite pitch	β and Φ

$$P_{O_{SESAM}} = \frac{1}{2}\rho_O V_{rel}^2 \left(\frac{2s^2+1}{\sqrt{\pi}s^3} \exp(-s^2) + \frac{4s^4+4s^2+1}{2s^4} \mathrm{erf}(s) \right) \tag{18}$$

where ρ_O is the NRLMSISE-00-based mass density of atomic oxygen, V_{rel} is the magnitude of the relative velocity vector, s is the speed ratio, exp is the exponential function, and erf is the Gauss error function. The speed ratio is defined as

$$s = \frac{V_{rel}}{\sqrt{\frac{m_O}{2k_B T_a}}} \tag{19}$$

where V_{rel} is the spacecraft relative velocity magnitude, m_O is the atomic mass of oxygen, k_B is the Boltzmann constant, and T_a is the atmospheric temperature.

The Langmuir parameter for SESAM appearing in Eq. (17) is obtained using

$$k_{L_{SESAM}} = s_o k_{L_{SESAM,o}} + k_{L_{SESAM,f}} \tag{20}$$

where $k_{L_{SESAM,o}}$ ($= 5 \times 10^6/133.322$ Pa^{-1}) is an 'initial' Langmuir parameter associated with circular orbits and $k_{L_{SESAM,f}}$ ($= 3 \times 10^4/133.322$ Pa^{-1}) is a 'final' Langmuir parameter associated with highly eccentric orbits. The parameter s_o is obtained from

$$s_o = \frac{s_{o_1}}{s_{o_2}} \tag{21a}$$

$$s_{o_1} = \sqrt{\pi k_B T_{ad} E_r}\left[\mathrm{erf}\left(\frac{\sqrt{E_b} - \sqrt{E_r}}{\sqrt{k_B T_{ad}}} \right) + \mathrm{erf}\left(\sqrt{\frac{E_r}{k_B T_{ad}}} \right) \right] + k_B T_{ad} \times \exp\left(-\frac{E_b + E_r}{k_B T_{ad}} \right) \left[\exp\left(\frac{E_b}{k_B T_{ad}} \right) - \exp\left(\frac{2\sqrt{E_b E_r}}{k_B T_{ad}} \right) \right] \tag{21b}$$

$$s_{o_2} = \sqrt{\pi k_B T_{ad} E_r}\left[\mathrm{erf}\left(\sqrt{\frac{E_r}{k_B T_{ad}}} \right) + 1 \right] + k_B T_{ad} \times \exp\left(-\frac{E_r}{k_B T_{ad}} \right) \tag{21c}$$

where T_{ad} (=93 K) is the transition temperature, E_r ($= 0.5 m_O V_{rel}^2$) is the incident kinetic energy of atomic oxygen, and E_b (=5.7 eV) is the adsorption energy.

The parameter α_{s_k} (the surface contribution to the effective energy accommodation coefficient) in Eq. (16) is obtained using

$$\alpha_{s_k} = 3\frac{\mu_k}{(1+\mu_k)^2} \tag{22}$$

where μ_k is the ratio of mass of species k to the mass of the particles that compose the satellite surface.

3. Derivation of thermosphere density estimates

Before the calibrated accelerations can be transformed into thermosphere density estimates, we first need to subtract the acceleration due to radiation pressure to obtain the aerodynamic acceleration,

$$\boldsymbol{a}_a = \boldsymbol{a}_c - \boldsymbol{a}_{rp} \tag{23}$$

where $\boldsymbol{a}_a$ is the aerodynamic acceleration vector, $\boldsymbol{a}_c$ is the calibrated acceleration vector, and $\boldsymbol{a}_{rp}$ is the radiation pressure acceleration vector. The latter comprises the effects of solar, albedo and Earth infrared radiation pressure (Doornbos, 2011). The aerodynamic acceleration can then be inserted into

$$\boldsymbol{a}_a = \frac{1}{2}\rho V_{rel}^2 \frac{A}{m} \boldsymbol{C}_a \tag{24}$$

where $\boldsymbol{C}_a$ is the aerodynamic coefficient vector. To obtain the thermosphere density, Eq. (24) is projected onto a suitably chosen unit vector $\boldsymbol{u}$. In this study, we chose $\boldsymbol{u}$ to be the direction of the relative velocity vector $\boldsymbol{V}_{rel}$, i.e.

$$\boldsymbol{u} = \frac{\boldsymbol{V}_{rel}}{V_{rel}}. \tag{25}$$

The relative velocity vector comprises the satellite velocity, the velocity of co-rotating atmosphere, and thermosphere wind (Doornbos, 2011). The first two are accurately known from precise orbit determination and Earth rotation, and for the last we use the HWM07 model (Drob et al., 2008). This particular choice of the unit vector $\boldsymbol{u}$ yields the drag acceleration

$$a_D = \boldsymbol{a}_a \cdot \frac{\boldsymbol{V}_{rel}}{V_{rel}} \tag{26}$$

and the drag coefficient

$$C_D = \boldsymbol{C}_a \cdot \frac{\boldsymbol{V}_{rel}}{V_{rel}}, \tag{27}$$

which allows us to derive thermosphere density according to

$$\rho = 2\frac{a_D m}{C_D V_{rel}^2 A}. \tag{28}$$

A peculiarity of the CHAMP accelerometer data is that the z-component, which is approximately pointing in the nadir direction, is inaccurate because of an instrument anomaly. Since Eq. (26) requires a complete acceleration vector as input, we replace the measured z-component in Eq. (24) with

$$a_{a,z} = \frac{C_{a,z}}{C_{a,x}} a_{a,x} \tag{29}$$

The effect of this replacement on the density observations is marginal because the x-axis of the satellite body is aligned with the flight direction within a few degrees.

4. Datasets

4.1. Satellite acceleration data

The input data for this study comes from the CHAMP, GRACE and GOCE satellites. The CHAMP (CHAllenging Minisatellite Payload) mission's objectives were the measurement of Earth's magnetic and gravity field (Reigber et al., 2002). For the latter, the satellite carried a dual-frequency GPS receiver and an electrostatic accelerometer. The purpose of the accelerometer was the measurement of the non-gravitational accelerations, so that the gravitational accelerations could be inferred from the GPS receiver data. In this paper, we use the non-gravitational accelerations to derive thermosphere density observations. The objective of the GRACE (Gravity Recovery And Climate Experiment) mission was to measure the gravity field, focusing on the time-variable instead of the mean field (Tapley et al., 2004). The GRACE satellites also carried accelerometers to measure the non-gravitational accelerations and a dual-frequency GPS receiver for precise orbit determination. The CHAMP and GRACE accelerometer data were calibrated by means of precise orbit determination, where gravitational accelerations were prescribed by models and the scale and bias of the accelerometer data were fitted to match the GPS receiver data (van Helleputte et al., 2009).

The GOCE (Gravity field and steady-state Ocean Circulation Explorer) satellite carried a gravity gradiometer consisting of six accelerometers. In contrast to the CHAMP and GRACE satellites, the GOCE satellite was equipped with a drag-free system, in which the non-gravitational acceleration measured by the gradiometer was used to control an ion engine to continuously counteract drag and maintain the extremely low altitude of 260 km (Floberghagen et al., 2011). Thus, the input data from the GOCE mission is the sum of the measured (residual) acceleration and the thrust of the ion engine divided by the mass of the satellite. Fig. 4 shows the altitude evolution of the CHAMP, GRACE, and GOCE satellites together with the F10.7 index, which is a proxy for solar activity in the Extreme Ultra Violet (EUV) spectral range. The parts of the orbits for which calibrated accelerations are available are shown in color while the grey parts are not yet calibrated. Nevertheless, the selected data sets cover the altitude range from about 500 km to 220 km as well as the full range of solar activity levels. This enables a comparison of the C_D modeling for all relevant conditions.

4.2. Thermosphere composition and temperature data

Satellite drag modeling requires thermosphere composition and temperature data. Since none of the CHAMP, GRACE, and GOCE satellites carried an instrument to measure these quantities, we rely on thermosphere models for that information. We use the NRLMSISE-00 model (Picone et al., 2002), which is based on mass spectrometer data and hence represents composition more accurately than other thermosphere models. In addition, the SESAM (Pilinski et al., 2013) and Walker models (Walker et al., 2014), which describe the energy accommodation coefficient as a function of the number density of atomic oxygen and atmospheric temperature, are compatible only with respective data from the NRLMSISE-00 model (Picone et al., 2002).

4.3. Existing derived density datasets

CHAMP, GRACE and GOCE amongst other missions in the thermosphere have provided a great amount of information for current density datasets. The first datasets were initiated by Bruinsma and Biancale (2003) and were followed by Sutton (2008)[1], Doornbos (2012), Calabia and Jin (2016)[2], Mehta et al. (2017)[3], and March et al. (2019a)[4]. For CHAMP and GRACE, other data sets have been generated for both simplified and more complex satellite geometries and different GSI assumptions (Bruinsma and Biancale, 2003; Sutton, 2008; Doornbos, 2011; Mehta et al., 2013; Mehta et al., 2014a).

For the latest datasets processed at TU Delft (DUT), some data are also available on the European Space Agency (ESA) servers. The two versions are identical except for the file format. On the TU Delft website, the data are provided together with geometry, aerodynamic models and lookup tables. Some of the processed missions also have crosswind data, as is the case for CHAMP and GOCE (March et al., 2019b). All the data are generated using the SPARTA simulator (previously mentioned in Section 2.2.2), and further improvements are foreseen due to updates to the radiation pressure modeling as well as GSI modeling following the recommendations of this paper. Presently, these datasets are generated for a constant energy accommodation coefficient using a DRIA reflections model. March et al. (2019b) analyzed GOCE and CHAMP crosswind observations to optimize the energy accommodation coefficient for these missions. For GOCE, the analysis of the seasonal variations of the zonal winds between −45° and +45° magnetic latitude revealed an optimal value of 0.82. The analysis of CHAMP crosswind observations focused on the attitude maneuver performed in November 2002, when the satellite was flying

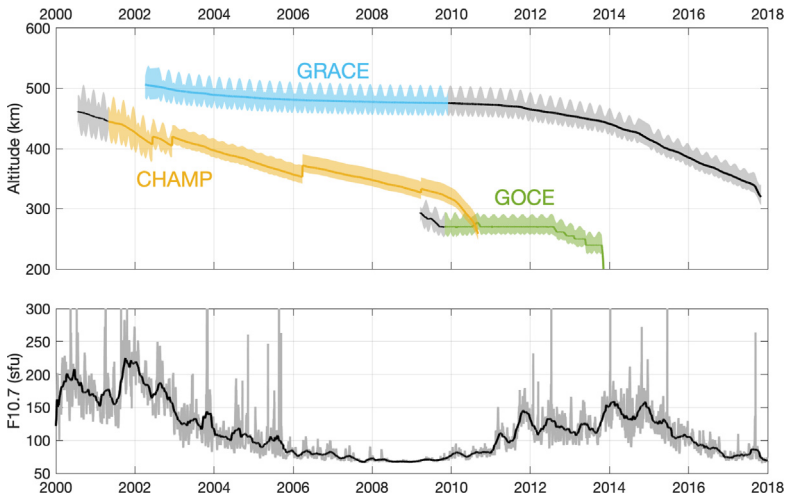

Fig. 4. Orbit evolution of the CHAMP, GRACE, and GOCE satellites (top) and solar activity as indicated by the F10.7 index (bottom). The grey data show the daily F10.7 index, while the black line refers to the 81-day average. In the top panel, color shows where calibrated accelerations are available, whereas grey is not calibrated.

sideways for a limited number of orbits, leading to a consistent optimal value of 0.85. For the GRACE satellites, no attempt has yet been made to find an optimal value of the energy accommodation coefficient. Instead, the value of 0.85 has been adopted, which may not be an optimal choice for the high altitude and the wide solar activity range encountered by GRACE.

The variability of satellite aerodynamic forces and mass density for different energy accommodation coefficients was also analyzed by March et al. (2021) using these aerodynamic data sets and simulations. In this work, the Swarm A and C satellites also turned out to provide more consistent density data for an energy accommodation coefficient of 0.85. Similarly to CHAMP, a manoeuvre analysis was introduced to retrieve this value. The final aerodynamic lookup tables and the high-fidelity geometry models are freely available[5].

Recent research efforts towards enhanced geometry and GSI modeling has improved the accuracy of density data sets (Pilinski et al., 2013; Pilinski et al., 2016; Mehta et al., 2017; March et al., 2021). Some of these new satellite surface geometries and GSI assumptions have been adopted in this work to address shortfalls in the definition of geometry features (e.g. baffles, antennas), and to enhance previous GSI assumptions. This is expected to provide a consistent overview of drag and density estimations without the main systematic errors that have affected previous datasets. The results presented herein aim to mitigate such effects by adopting common high-fidelity geometries from March et al. (2019a) (Fig. 2) allowing focus to turn to the remaining features driven by the use of different modeling methods.

5. Results and discussion

In this section, we compare first the drag coefficients for the GSI models discussed in Section 2, calculated with computational methods described there. Next, we compare the resulting density estimates, first to an arbitrary reference density in Section 5.2, for which the DUT-DRIA-0.85 (GRACE and CHAMP) and DUT-DRIA-0.82 (GOCE) densities were selected, and secondly to the (semi-empirical) thermosphere models NRLMSISE-00 (Picone et al., 2002) and DTM2020 (Bruinsma and Boniface, 2021) in Section 5.3.

5.1. Drag coefficients

In Fig. 5, we present the C_D (left panels) and the α for helium and atomic oxygen with RSM-DRIA-SESAM as well as θ for atomic oxygen with RSM-DRIA-WLK and RSM-CLL-WLK (right panels). For GOCE, the largest difference in C_D of about 10% is between DUT-DRIA-0.85 and RSM-CLL-WLK. The difference between C_D (and so densities too) obtained with DRIA does not exceed 6%. For CHAMP, all C_D are very similar, and differences do not exceed 3%. For GRACE, orbiting at the highest altitude (cf. Fig. 4) where helium and atomic oxygen are the major constituents, the C_D are quite different. The largest difference, ranging from a few percent at solar maximum in 2002 to about 30% at solar minimum in 2008–2009, is between RSM-CLL-WLK and DUT-DRIA-0.85. Differences between the employed DRIA models are smaller, but still increase from about 4% at solar maximum to 13% at solar minimum. The differences in the C_D can be explained by the accommodation model employed. SESAM and Walker models strongly depend on the solar

[1] http://sisko.colorado.edu/sutton/data/ver2.
[2] https://zenodo.org/record/4308315.
[3] http://tinyurl.com/densitysets.
[4] http://thermosphere.tudelft.nl.

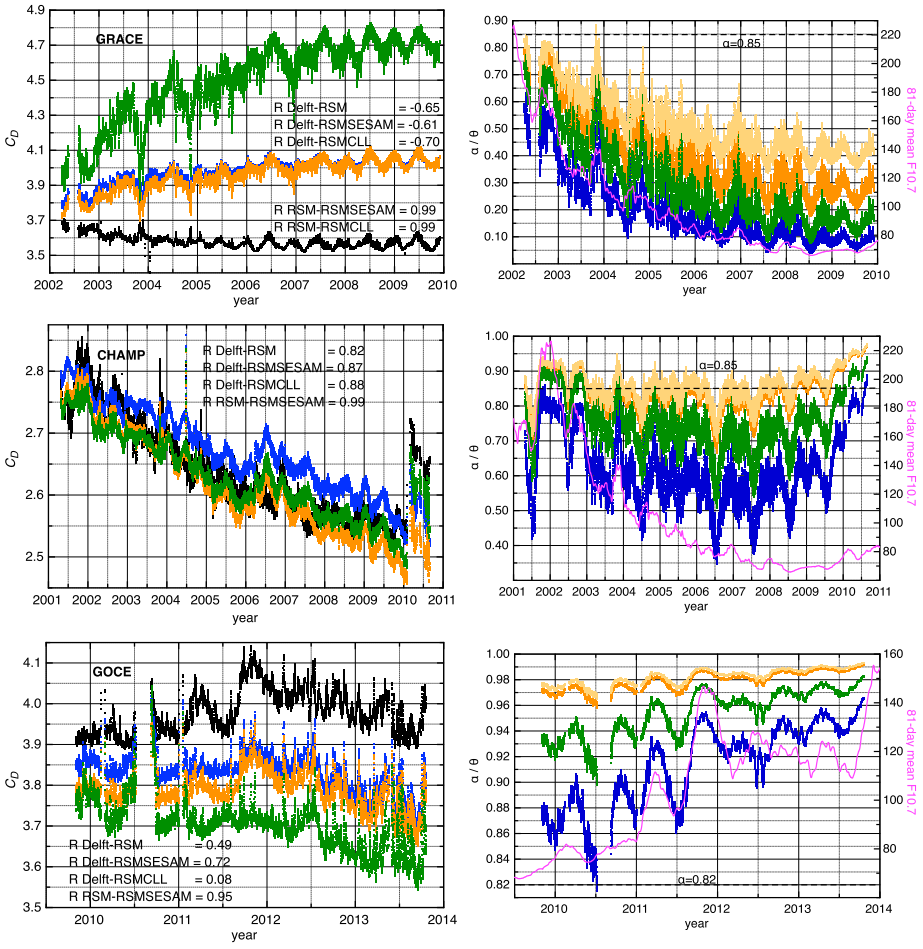

Fig. 5. The drag coefficients (left frames) and accommodation and RSM θ (right frames) for GRACE (top frames), CHAMP (middle frames) and GOCE (bottom frames): DUT-DRIA (black), RSM-DRIA-WLK (dark blue), RSM-CLL-WLK(green), RSM-DRIA-SESAM (orange). The accommodation with SESAM is calculated for helium (orange) and atomic oxygen (yellow). Note: DUT uses α of 0.82 for GOCE and 0.85 for GRACE and CHAMP.

activity, which modulates the atomic oxygen and helium concentrations. This effect is not very-well visible for CHAMP, because the orbit decay partly compensated the effect of the decreasing solar activity. For GRACE, the correlation is evident and explains the differences in C_D.

It should be noted that we did not test the sensitivity of the C_D and, therefore, derived density estimates to potential errors in the atmospheric composition and temperature, which are calculated from the NRLMSISE-00 model.

5.2. Comparison with TU Delft Density Estimates

The comparisons are done by computing daily-mean density ratios in order to clearly determine trends and variations related to altitude and solar activity. Fig. 6 presents the daily-mean density ratios of GRACE (top frame), CHAMP, and GOCE (bottom frame) for ADB-DRIA-0.85 (0.82 for GOCE), RSM-CLL-WLK for the sake of completeness, and the following three RSM-DRIA realizations: RSM-DRIA-WLK, RSM-DRIA-0.85 or RSM-DRIA-0.82, and RSM-DRIA-SESAM.

Of the three satellites, GOCE, at the lowest altitude, orbited in the most atomic oxygen-rich environment. Compared to DUT-DRIA-0.82, significant differences in the densities are revealed, ranging from an almost constant 9.6% smaller ADB-DRIA-0.82 density, via 1% to 6% larger RSM-DRIA-WLK and RSM-DRIA-SESAM densities, to 4% to 10% larger RSM-CLL-WLK densities. The RSM-DRIA-WLK and RSM-DRIA-SESAM density ratios present a trend that is indicative of their increasing accommodation compared to the constant value of 0.82. The majority of the ADB-DRIA-0.82 GOCE density offset is due to the panel method employed. The RSM-DRIA-0.82 and RSM-DRIA-0.85 were computed to check the agreement with DUT-DRIA-0.82, which is verified, even if a weak trend of about 1% over the 4 years is visible.

For CHAMP, the RSM-DRIA-0.85 also agrees very well with DUT-DRIA-0.85 densities, but again a weak slope of about −1% over 9 years is visible. The ADB-DRIA-0.85 densities, with a weak slope of about 1% over 9 years, agree very well too. The mean offset of RSM-

[5] http://thermosphere.tudelft.nl.

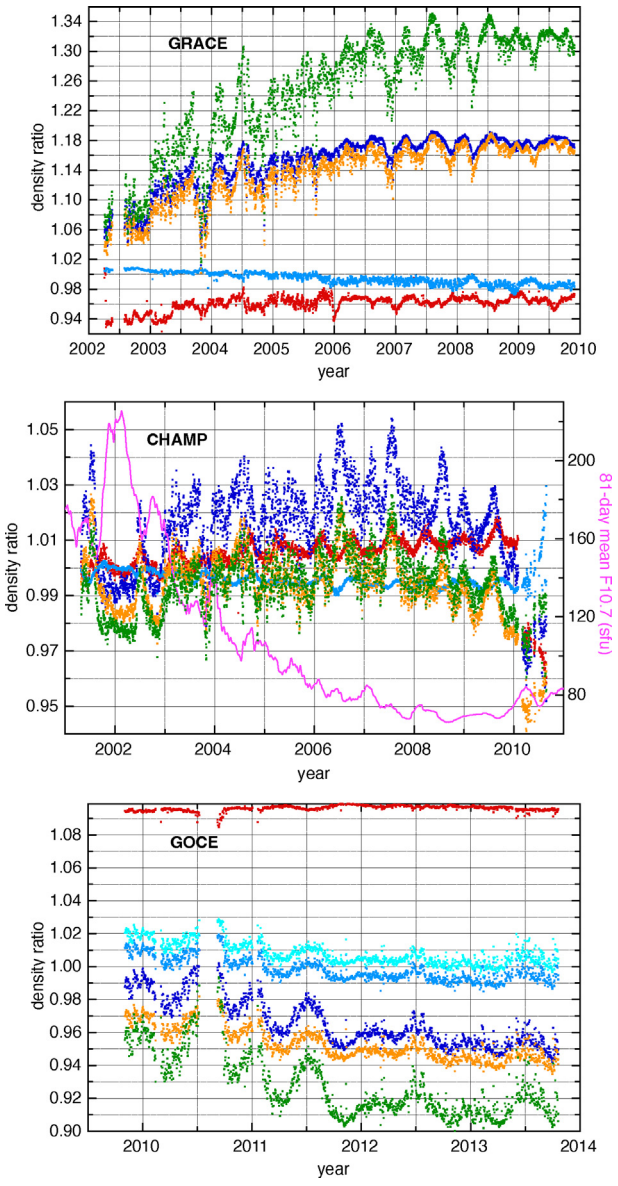

Fig. 6. Daily-mean density ratios of DUT-DRIA to GRACE (top), CHAMP and GOCE (bottom) for: RSM-DRIA-WLK (dark blue), RSM-DRIA-0.85 (blue), RSM-DRIA-0.82 (light blue), RSM-CLL-WLK (green), RSM-DRIA-SESAM (orange) and ADB-DRIA (red). Note: ADB and DUT use α of 0.82 for GOCE and 0.85 for GRACE and CHAMP.

DRIA-WLK is 1.5%, and variations in solar activity cause the fluctuations with a maximum of 1% peak-to-peak. The average offset of RSM and RSM SESAM is 1.5% and −0.5%, respectively, but the ratios are more sensitive to variations in solar activity (e.g. the peak centered on 2002), which cause variations in the atomic oxygen concentration. The RSM-CLL-WLK ratios present a similar progression. RSM-DRIA-WLK density ratios fluctuate most strongly, up to 5% peak-to-peak (standard deviation SD = 1.6%), while RSM-DRIA-SESAM ratios present similar, but slightly weaker fluctuations. The ratios in 2010 present fast fluctuations, with steep slopes or even discontinuities, also when another reference is selected. The discontinuities are related to the change in satellite attitude in February 2010. Before, CHAMP was orbiting with the boom pointing into flight direction, and after with the boom pointing into anti-flight direction. In the final year of the mission, its altitude decayed from about 300 km to atmospheric re-entry in 10 months.

The mean altitude of GRACE was 475 km from 2002–2009. Concentration of atomic oxygen falls off over that period from solar maximum to minimum, while helium concentration increases in particular over the winter poles. The declining atomic oxygen levels are reflected in the sharp, nearly identical increase of about 10% of RSM-DRIA-WLK and RSM-DRIA-SESAM ratios from 2002–2005, while the total difference in 2009 reaches about 18%. RSM-CLL-WLK is most sensitive to atomic oxygen, and the largest difference in the ratios of about 30% is revealed. RSM-DRIA-0.85 agrees well with DUT-DRIA-0.85 densities with a mean offset of −1% and weak slope of about −1% over 8 years. The ratios show that ADB-DRIA-0.85 densities are on average 3.7% larger, and 6% larger in 2002.

5.3. Comparison with NRLMSISE-00 and DTM2020 Models

The satellite density data are compared with NRLMSISE-00 and DTM2020-F107 densities in order to demonstrate the effect of fitting thermosphere models to their own distinct density datasets. Both models use the same drivers for solar and geomagnetic activity, but DTM2020 was fitted to GOCE, CHAMP and GRACE data (somewhat older versions of the DUT GOCE and CHAMP data, which are essentially 5% smaller than the data presented here, while CNES GRACE data was used), whereas NRLMSISE-00 was developed before the launch of those satellites. The mean observed-to-model density ratios are computed per year. Fig. 7 presents the yearly-mean density ratios of GRACE (top frame), CHAMP, and GOCE (bottom frame) for DUT-DRIA-0.85 (0.82 for GOCE), ADB-DRIA-0.85 (0.82 for GOCE), RSM-DRIA-WLK, RSM-DRIA-0.85, RSM-DRIA-SESAM, and RSM-CLL-WLK. The much larger biases of NRLMSISE-00, when comparing the left and right columns, are obvious. A second feature that stands out is the solar cycle signature in the density ratios of CHAMP, the rather steep slopes for GOCE, which are even steeper but of opposite sign in case of GRACE. These differences are due to fitting to distinct density data, which appear to be incompatible with GOCE, CHAMP and GRACE.

The GOCE-to-DTM2020-F107 density ratios present the lowest standard deviations (SD), and are smallest for RSM-DRIA-SESAM (0.9%) and RSM-DRIA-WLK (1.1%). DTM2020-F107 was fitted to GOCE density data from TU Delft, not exactly the same data used in this study, but with a constant accommodation coefficient of 0.85. The SD of the DUT-GOCE-0.82 densities is signifi-

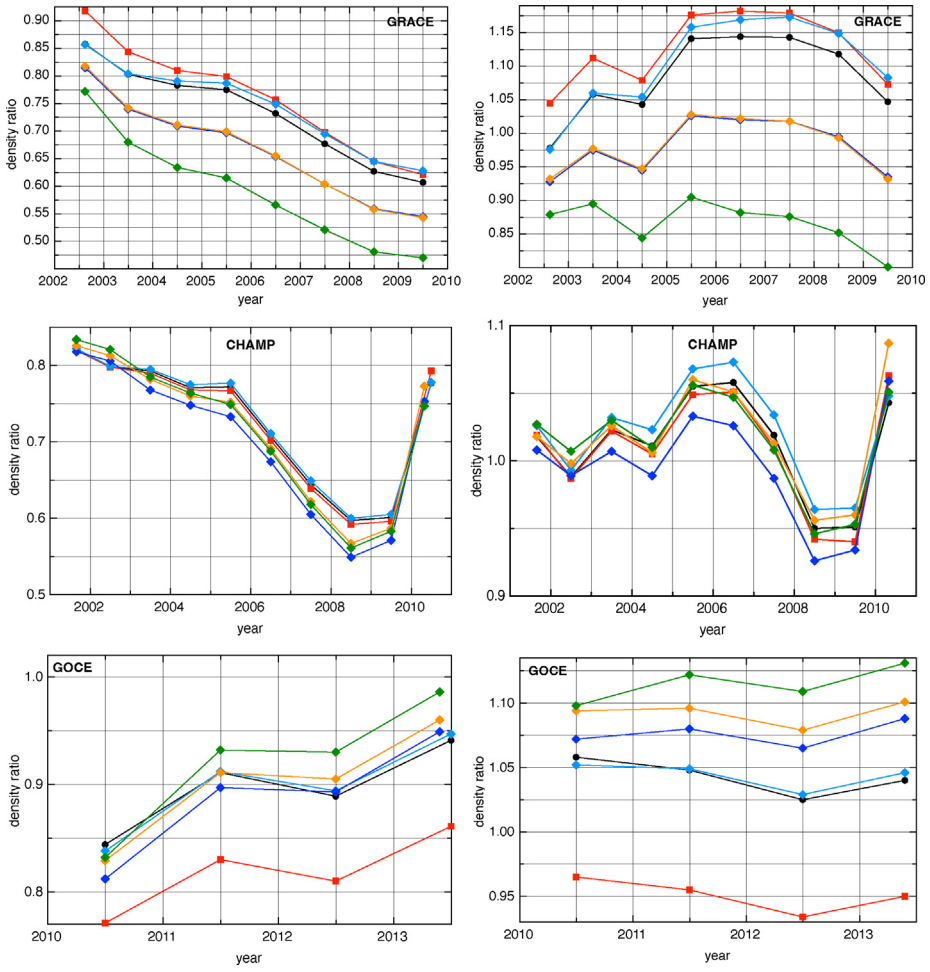

Fig. 7. Yearly-mean ratios of observed density to NRLMSISE-00 (left frames) and DTM-2020 (right frames) models for: RSM-DRIA-WLK (dark blue), RSM-DRIA-0.85 (blue), RSM-CLL-WLK (green), RSM-DRIA-SESAM (orange), DUT-DRIA (black), and ADB-DRIA (red). Note: ADB and DUT use α of 0.82 for GOCE and 0.85 for GRACE and CHAMP. GRACE ratios are shown in top frames, CHAMP in middle frames, and GOCE in bottom frames.

cantly larger (1.3%), which seems to indicate the incorrectness of this assumption. For CHAMP, the SD and biases are all very similar. For GRACE, which experienced the largest variations in atomic oxygen and helium, and therefore the largest variations in α according to RSM-DRIA-SESAM or RSM-DRIA-WLK, the SD of the density ratios are again significantly smaller with RSM-DRIA-SESAM and RSM-DRIA-WLK (4.1% for both) compared with DUT-DRIA-0.85 (5.9%). For CHAMP, all densities are comparable, including the RSM-CLL-WLK densities. At the GOCE altitude, the RSM-CLL-WLK densities are a few percent larger than RSM-DRIA-WLK and RSM-DRIA-SESAM, and almost 10% larger than DUT-DRIA-0.85 densities. For GRACE, the RSM-CLL-WLK densities are considerably smaller than RSM-DRIA-WLK or RSM-DRIA-SESAM, and the density ratios become very small, respectively 0.47 and 0.80 for NRLMSISE-00 and DTM2020-F107 in 2009.

6. Conclusions and recommendations

This paper presents a first comprehensive comparison of the different methods for computation of satellite drag coefficients and the impacts on the density estimates derived from in situ measurements of acceleration. It is observed that the differences in the modeled drag coefficients and hence the derived density estimates are tens of percent in some cases. Thus, data users (e.g. modelers) should be careful when using datasets for scientific investigations, particularly when combining data sets from different sources or spanning a wide range of altitudes and solar activity levels. The differences are largest near solar minimum conditions at higher altitudes (i.e., above 450 km) and are a result of the widely varying approach to modeling the accommodation coefficient(s) (e.g. a constant value vs SESAM).

Based on GOCE and CHAMP, we also conclude that the use of a constant value for accommodation coefficient (s) is likely valid below about 400 km in altitude and cer-

tain solar conditions depending on the acceptable range of differences (<5%). However, we suggest that this should be reevaluated in the future within the context of development of new materials and availability of in situ measurements and observations. Nevertheless, we recommend the use of a variable accommodation model to account for the effects of changes in composition and temperature for all altitudes and solar conditions. We conclude and recommend that the community needs to arrive at a consensus on the appropriate models for accommodation coefficient.

While we do not analyze data at altitudes above 500 km, the nature of GSI at higher altitudes where most of our Earth observation assets reside, remains unclear. Even if the effect of atmospheric drag on the orbit becomes small, for some satellites with stringent ground track requirements the associated error remains important. Secondly, the choice of GSI model can change the calculated drag significantly, and this has serious consequences for mission design and re-entry calculations. Presently, we have very few satellites above 500 km altitude that we can use to derive density estimates, and even then only orbit-mean or daily-mean densities. More missions in the 500 km to 800 km altitude range are necessary to enable both more accurate drag coefficient as well as thermosphere modeling.

To account for the errors introduced by these datasets in the modeling efforts, we conclude and recommend that any further developments include robust uncertainty quantification. To minimize these errors, we recommend that the community reach a consensus for a baseline tool for modeling drag coefficient.

The accuracy of variable accommodation models could be improved by using in situ observations. We outline here a mission concept that would be suited to constrain variable accommodation models with much greater accuracy than is possible with existing measurements. The mission should consist of two satellites flying in the same orbit, separated by a distance of about 100 km. We consider this distance to be short enough such that both satellite experience nearly identical density along the orbit while still maintaining a safe distance. The orbit should be elliptical, so that measurements are collected in the altitude range of 350 km to 600 km to cover both atomic oxygen- and helium-dominated regimes. The instruments on board the satellites should include an accelerometer and a precise GNSS receiver for accelerometer data calibration, which together provide the calibrated acceleration $\boldsymbol{a}_c$ in Eq. (23). Further, a mass spectrometer should be included to measure atmospheric composition and temperature, and to obtain independent observations of mass density. Ram and cross wind sensors should be included since wind is part of the relative velocity $\boldsymbol{V}_r$. The two satellites should be identical and elongated, and orbit nominally with the small cross-section pointing into the flight direction (0° yaw angle). However, they should have the capability to fly at a yaw angle of 90° (sideways), such that the area of the perpendicular and parallel surfaces with respect to the flow will essentially be inverted by such a manoeuvre, which will change the contributions of the normal and tangential accommodation (Bernstein et al., 2021). Then, the data collected during periods when the two satellites are flying in different orientations could be studied in a similar way as the attitude maneuver analysis for the Swarm mission by March et al. (2021), avoiding any use of a thermosphere models. The difference in the contributions of the normal and tangential accommodation to the drag coefficient in combination with the satellites experiencing the same density due to their close proximity, will allow to constrain variable accommodation models.

Declaration of Competing Interest

The authors declare that they have no known competing financial interests or personal relationships that could have appeared to influence the work reported in this paper.

Acknowledgements

PMM gratefully acknowledges support under NSF CAREER award #2140204. GM and CS would like to thank the European Space Agency for supporting the production of GOCE density estimates (Contract 766 18308/04/NL/MM), which are made available by ESA (https://earth.esa.int/eogateway/). Further, GM and CS gratefully acknowledge the support by the Netherlands Organisation for Scientic Research (NWO, project number ALW-GO/14–35), which enabled the creation of the CAD models of the satellites and the DUT density estimates available at http://thermosphere.tudelft.nl. SB is supported by CNES APR grant METEOESP.

References

Bernstein, V., Pilinski, M., Knipp, D., 2021. Drag coefficient constraints for space weather observations in the upper thermosphere. J. Spacecraft Rock. 57 (6), 1246–1263. https://doi.org/10.1002/essoar.10508667.1.

Bettadpur, S., 2012. GRACE 327–720 (CSR-GR-03-02), Gravity Recovery and Climate Experiment. Product Specification Document (Rev 46).

Bird, G.A., 1994. Molecular Gas Dynamics and the Direct Simulation of Gas Flows. Clarendon Press, Oxford, UK.

Boniface, C., Bruinsma, S., 2021. Uncertainty quantification of the DTM2020 thermosphere model. J. Space Weather Space Climate 11 (53). https://doi.org/10.1051/swsc/2021034.

Bruinsma, S., Biancale, R., 2003. Total Densities Derived from Accelerometer Data. J. Spacecraft Rock. 40 (2), 230–236. https://doi.org/10.2514/2.3937.

Bruinsma, S., Boniface, C., 2021. The operational and research DTM-2020 thermosphere models. J. Space Weather Space Climate 11 (47). https://doi.org/10.1051/swsc/2021032.

Calabia, A., Jin, S., 2016. New modes and mechanisms of thermospheric mass density variations from GRACE accelerometers. J. Geophys. Res.: Space Phys. 121 (11), 11,191–11,212. https://doi.org/10.1002/2016JA022594.

Comsa, G., Fremerey, J.K., Lindenau, B., Messer, G., Röhl, P., 1980. Calibration of a spinning rotor gas friction gauge against a fundamental vacuum pressure standard. J. Vacuum Sci. Technol. 17 (2), 642–644. https://doi.org/10.1116/1.570531.

Davis, D.H., 1960. Monte Carlo calculation of molecular flow rates through a cylindrical elbow and pipes of other shapes. J. Appl. Phys. 31 (7), 1169–1176. https://doi.org/10.1063/1.1735797.

Doornbos E. Thermospheric Density and Wind Determination From Satellite Dynamics. PhD thesis.; Department of Astrodynamics and Satellite Missions, Delft University of Technology; 2011.

Doornbos, E., 2012. Producing density and crosswind data from satellite dynamics observations. In: Thermospheric Density and Wind Determination from Satellite Dynamics. Berlin, Heidelberg: Springer, Berlin Heidelberg. p. 91–126. https://doi.org/10.1007/978-3-642-25129-0_4.

Doornbos, E., Klinkrad, H., Visser, P., 2008. Use of two-line element data for thermosphere neutral density model calibration. Adv. Space Res. 41 (7), 1115–1122. https://doi.org/10.1016/j.asr.2006.12.025, URL: https://www.sciencedirect.com/science/article/pii/S0273117706007836.

Drob, D.P., Emmert, J.T., Crowley, G., Picone, J.M., Shepherd, G.G., Skinner, W., Hays, P., Niciejewski, R.J., Larsen, M., She, C.Y., Meriwether, J.W., Hernandez, G., Jarvis, M.J., Sipler, D.P., Tepley, C. A., O'Brien, M.S., Bowman, J.R., Wu, Q., Murayama, Y., Kawamura, S., Reid, I.M., Vincent, R.A., 2008. An empirical model of the Earth's horizontal wind fields: HWM07. J. Geophys. Res.: Space Phys. 113 (A12304). https://doi.org/10.1029/2008JA013668.

Emmert, J.T., 2009. A long-term data set of globally averaged thermospheric total mass density. J. Geophys. Res.: Space Phys. 114 (A6), A06315. https://doi.org/10.1029/2009JA014102.

Floberghagen, R., Fehringer, M., Lamarre, D., Muzi, D., Frommknecht, B., Steiger, C., Piñeiro, J., da Costa, A., 2011. Mission design, operation and exploitation of the gravity field and steady-state ocean circulation explorer mission. J. Geodesy 85, 749–758. https://doi.org/10.1007/s00190-011-0498-3.

Fredo, R.M., Kaplan, M.H., 1981. Procedure for obtaining aerodynamic properties of spacecraft. J. Spacecraft Rock. 18 (4), 367–373. https://doi.org/10.2514/3.28061, URL: https://arc.aiaa.org/doi/10.2514/3.28061.

Fuller, J.D., Tolson, R.H., 2009. Improved Method for the Estimation of Spacecraft Free-Molecular Aerodynamic Properties. J. Spacecraft Rock. 46 (5), 938–948. https://doi.org/10.2514/1.43205, URL: https://arc.aiaa.org/doi/10.2514/1.43205.

Gallis, M., Torczynski, J., Plimpton, S., Rader, D., Koehler, T., 2014. Direct simulation Monte Carlo: the quest for speed. In: AIP Conference Proceedings (Editor: Fan, Jing) vol. 1628, pp. 27–36. https://doi.org/10.1063/1.4902571.

Goodman, F.O., 1977. Preliminary results of three-dimensional hard-sphere theory of scattering of gas atoms from a solid surface. In: Brundin C.L, (Ed.), Proceedings of the 5th International Symposium on Rarefied Gas Dynamics held at the University of Oxford, pp. 35–48.

van Helleputte, T., Doornbos, E., Visser, P., 2009. CHAMP and GRACE accelerometer calibration by GPS-based orbit determination. Adv. Space Res. 43 (12), 1890–1896. https://doi.org/10.1016/j.asr.2009.02.017.

Klinkrad, H., Koeck, C., Renard, P., 1990. Precise satellite skin-force modelling by means of Monte-Carlo ray tracing. ESA Journal 14 (4), 409–430.

Lord, R.G., 1991. Some extensions to the Cercignani-Lampis gas–surface scattering kernel. Phys. Fluids A 3 (4), 706–710. https://doi.org/10.1063/1.858076.

March, G., Doornbos, E., Visser, P., 2019a. High-fidelity geometry models for improving the consistency of CHAMP, GRACE, GOCE and Swarm thermospheric density data sets. Adv. Space Res. 63 (1), 213–238. https://doi.org/10.1016/j.asr.2018.07.009.

March, G., van den IJssel, J., Siemes, C., Visser, P., Doornbos, E., Pilinski, M., 2021. Gas-surface interactions modelling influence on satellite aerodynamics and thermosphere mass density. J. Space Weather Space Climate 11 (54). https://doi.org/10.1051/swsc/2021035.

March, G., Visser, T., Visser, P., Doornbos, E., 2019b. CHAMP and GOCE thermospheric wind characterization with improved gas-surface interactions modelling. Adv. Space Res. 64 (6), 1225–1242. https://doi.org/10.1016/j.asr.2019.06.023.

Mehta, P.M., Linares, R., 2020. Real-time thermospheric density estimation from satellite position measurements. J. Guidance, Control, Dyn. 43 (9), 1656–1670. https://doi.org/10.2514/1.G004793.

Mehta, P.M., Linares, R., Sutton, E.K., 2019. Data-driven inference of thermosphere composition during solar minimum conditions. Space Weather 17 (9), 1364–1379. https://doi.org/10.1029/2019SW002264.

Mehta, P.M., McLaughlin, C.A., Sutton, E.K., 2013. Drag coefficient modeling for GRACE using Direct Simulation Monte Carlo. Adv. Space Res. 52 (12), 2035–2051. https://doi.org/10.1016/j.asr.2013.08.033.

Mehta, P.M., Walker, A., Lawrence, E., Linares, R., Higdon, D., Koller, J., 2014a. Modeling satellite drag coefficients with response surfaces. Adv. Space Res. 54 (8), 1590–1607. https://doi.org/10.1016/j.asr.2014.06.033.

Mehta, P.M., Walker, A., McLaughlin, C.A., Koller, J., 2014b. Comparing physical drag coefficients computed using different gas–surface interaction models. J. Spacecraft Rock. 51 (3), 873–883. https://doi.org/10.2514/1.A32566.

Mehta, P.M., Walker, A.C., Sutton, E.K., Godinez, H.C., 2017. New density estimates derived using accelerometers on board the CHAMP and GRACE satellites. Space Weather 15 (4), 558–576. https://doi.org/10.1002/2016SW001562.

Moe, K., Moe, M.M., 2005. Gas–surface interactions and satellite drag coefficients. Planet. Space Sci. 53 (8), 793–801. https://doi.org/10.1016/j.pss.2005.03.005, URL: https://www.sciencedirect.com/science/article/pii/S0032063305000486.

Moe, K., Moe, M.M., Wallace, S.D., 1998. Improved satellite drag coefficient calculations from orbital measurements of energy accommodation. J. Spacecraft Rock. 35 (3), 266–272. https://doi.org/10.2514/2.3350.

Moe, M.M., Moe, K., 1969. The roles of kinetic theory and gas-surface interactions in measurements of upper-atmospheric density. Planet. Space Sci. 17 (5), 917–922. https://doi.org/10.1016/0032-0633(69)90097-X.

Moe, M.M., Wallace, S.D., Moe, K., 1995. Recommended drag coefficients for aeronomic satellites. In: Johnson, R.M., Killeen, T.L. (Eds.), The Upper Mesosphere and Lower Thermosphere: A Review of Experiment and Theory. American Geophysical Union (AGU), pp. 349–356, https://doi.org/10.1029/GM087p0349. URL: https://agupubs.onlinelibrary.wiley.com/doi/abs/10.1029/GM087p0349.

Mostaza-Prieto, D., 2017. Characterisation and Applications of Aerodynamic Torques on Satellites. PhD thesis.; School of Mechanical, Aerospace and Civil Engineering, The University of Manchester.

Picone, J.M., Hedin, A.E., Drob, D.P., Aikin, A.C., 2002. NRLMSISE-00 empirical model of the atmosphere: Statistical comparisons and scientific issues. J. Geophys. Res.: Space Phys. 107 (A12), 1468. https://doi.org/10.1029/2002JA009430.

Pilinski, M.D., Argrow, B.M., Palo, S.E., 2010. Semi-empirical model for satellite energy accommodation coefficients. J. Spacecraft Rock. 47 (6), 951–956. https://doi.org/10.2514/1.49330.

Pilinski, M.D., Argrow, B.M., Palo, S.E., 2013. Semi-empirical satellite accommodation model for spherical and randomly tumbling objects. J. Spacecraft Rock. 50 (3), 556–571. https://doi.org/10.2514/1.A32348.

Pilinski, M.D., Bowman, B.A., Palo, S.E., Forbes, J.M., Davis, B.L., Moore, R.G., Koehler, C., Sanders, B., 2016. Comparative Analysis of Satellite Aerodynamics and Its Application to Space-Object Identification. Adv. Space Res. 53 (5), 1–11. https://doi.org/10.2514/1.A33482.

Porodnov, B.T., Suetin, P.E., Borisov, S.F., Akinshin, V.D., 1974. Experimental investigation of rarefied gas flow in different channels. J. Fluid Mech. 64 (3), 417–438. https://doi.org/10.1017/S0022112074002485.

Reigber, C., Lühr, H., Schwintzer, P., 2002. CHAMP mission status. Adv. Space Res. 30 (2), 129–134. https://doi.org/10.1016/S0273-1177(02)00276-4.

Sentman, L.H., 1961. Free molecule flow theory and its application to the determination of aerodynamic forces. Technical Report; LOCKHEED MISSILES AND SPACE CO INC SUNNYVALE CA.

Sheridan, P.L., Paul, S.N., Avendāno Franco, G., Mehta, P.M., 2022. Updates and improvements to the satellite drag coefficient Response Surface Modeling toolkit. Adv. Space Res. 69 (10), 3828–3846. https://doi.org/10.1016/j.asr.2022.02.044.

Sinpetru, L.A., Crisp, N.H., Mostaza-Prieto, D., Livadiotti, S., Roberts, P.C.E., 2022a. ADBSat: Methodology of a novel panel method tool for aerodynamic analysis of satellites. Comput. Phys. Commun. 275, 108326. https://doi.org/10.1016/j.cpc.2022.108326, URL: https://linkinghub.elsevier.com/retrieve/pii/S0010465522000443.

Sinpetru, L.A., Crisp, N.H., Roberts, P.C.E., Sulliotti-Linner, V., Hanessian, V., Herdrich, G.H., Romano, F., Garcia-Almiñana, D., Rodríguez-Donaire, S., Seminari, S., 2022b. ADBSat: Verification and validation of a novel panel method for quick aerodynamic analysis of satellites. Comput. Phys. Commun. 275, 108327. https://doi.org/10.1016/j.cpc.2022.108327, URL: https://linkinghub.elsevier.com/retrieve/pii/S0010465522000455.

Storz, M., Bowman, B., Branson, J., 2005. High Accuracy Satellite Drag Model (HASDM). In: AIAA/AAS Astrodynamics Specialist Conference and Exhibit. https://doi.org/10.2514/6.2002-4886. URL: https://arc.aiaa.org/doi/abs/10.2514/6.2002-4886. arXiv:https://arc.aiaa.org/doi/pdf/10.2514/6.2002-4886.

Suetin, P.E., Porodnov, B.T., Chernjak, V.G., Borisov, S.F., 1973. Poiseuille flow at arbitrary knudsen numbers and tangential momentum accommodation. J. Fluid Mech. 60 (3), 581–592. https://doi.org/10.1017/S0022112073000352.

Sutton, E.K., 2008. Effects of solar disturbances on the thermosphere densities and winds from CHAMP and GRACE satellite accelerometer data. PhD thesis.; Department of Aerospace Engineering Sciences, University of Colorado at Boulder.

Tapley, B.D., Bettadpur, S., Watkins, M., Reigber, C., 2004. The gravity recovery and climate experiment: Mission overview and early results. Geophys. Res. Lett. 31 (9), L09607. https://doi.org/10.1029/2004GL019920.

Thayer, J.P., Liu, X., Lei, J., Pilinski, M., Burns, A.G., 2012. The impact of helium on thermosphere mass density response to geomagnetic activity during the recent solar minimum. J. Geophys. Res.: Space Phys. 117 (A7), A07315. https://doi.org/10.1029/2012JA017832.

Walker, A., Mehta, P., Koller, J., 2013. The effect of different adsorption models on satellite drag coefficients. In: AIAA/AAS Astrodynamics Specialist Conference. AAS 13–746.

Walker, A., Mehta, P., Koller, J., 2014. Drag coefficient model using the Cercignani–Lampis–Lord gas–surface interaction model. J. Spacecraft Rock. 51 (5), 1544–1563. https://doi.org/10.2514/1.A32677.

Xu, J., Wang, W., Lei, J., Sutton, E., Chen, G., 2011. The effect of periodic variations of thermospheric density on CHAMP and GRACE orbits. J. Geophys. Res. 116 (A2), A02315. https://doi.org/10.1029/2010JA015995.

Yamazaki, Y., Kosch, M.J., Sutton, E.K., 2015. A model of high-latitude thermospheric density. J. Geophys. Res.: Space Phys. 120 (9), 7903–7917. https://doi.org/10.1002/2015JA021371.

Yang, Y.M., Meng, X., Komjathy, A., Verkholyadova, O., Langley, R.B., Tsurutani, B.T., J.MA, 2014. Tohoku-Oki earthquake caused major ionospheric disturbances at 450 km altitude over Alaska. Radio Sci. 49 (12), 1206–1213. https://doi.org/10.1002/2014RS005580.